Visualization of β-Sheets and Side-Chain Clusters in Two-Dimensional Periodic Arrays of Streptavidin on Phospholipid Monolayers by Electron Crystallography

Agustin J. Avila-Sakar* and Wah Chiu*‡
*Department of Molecular Physiology and Biophysics, ‡Verna and Marrs McLean Department of Biochemistry, The W. M. Keck Center for Computational Biology, Baylor College of Medicine, Houston, Texas 77030 USA

ABSTRACT The biotin-binding protein streptavidin was crystallized as two-dimensional periodic arrays on biotinylated phospholipid monolayers. Electron diffraction patterns and images of the arrays embedded in vitreous ice were recorded to near-atomic resolution. Amplitudes and phases of structure factors were computed and combined to produce a 3 Å projection density map. The reliability of the map was verified by comparing it to the available x-ray atomic model of the molecule. Projection densities from β-strands and some amino acid side chains were identified from the electron cryomicroscopy map. These results demonstrate the first near-atomic image of this type of protein periodic array by electron crystallography, which has a great potential to aid in the structural characterization of molecular arrays engineered on a monolayer for various basic or biotechnological applications.

INTRODUCTION

Two-dimensional (2-D)[1] protein crystallization on lipid monolayers was introduced over a decade ago as a novel technique to solve the structure of biological macromolecules (Fromherz, 1971; Uzgiris and Kornberg, 1983). It has stimulated the development of functionalized surfaces for molecular devices, such as biosensors (Ahlers et al., 1989; Morgan and Taylor, 1992). It has also been proposed as a model system to study surface recognition phenomena, analogous to the type presumably occurring at cell membranes between ligands and receptors (Ahlers et al., 1990; Blankenburg et al., 1989; Müller et al., 1993). In addition, it has recently been demonstrated to be a useful seeding technique for the epitaxial growth of x-ray quality crystals (Hemming et al., 1995). Among more than a dozen proteins (Kornberg and Darst, 1991; Jap et al., 1992) or macromolecular assemblies (Avila-Sakar et al., 1994) that have been crystallized by this technique, streptavidin 2-D crystals diffract electrons beyond 3 Å (Kubalek et al., 1991), suggesting that structure may be retrievable at that resolution. This 15 kDa protein, synthesized by *Streptomyces avidinii*, is probably the single most widely used protein in modern biochemical assays (Bayer and Wilchek, 1990). Because of its extremely high affinity ($K_d \approx 10^{-15}$ M) for the vitamin biotin (Green, 1975; Garlick and Giese, 1988), it forms nearly irreversible complexes, which can be detected by a variety of methods (Bayer and Wilchek, 1990). The atomic structure of streptavidin was solved independently by Weber et al. (1989) and Hendrickson et al. (1989) using x-ray crystallographic methods. The availability of an atomic model of the protein made streptavidin a suitable test specimen for evaluating the merits of electron crystallography for retrieving high-resolution structure from 2-D protein periodic arrays on lipid monolayers.

MATERIALS AND METHODS

Specimen preparation

Streptavidin was purchased from Boheringer Mannheim GmbH (Mannheim, Germany). Dioleoylphosphatidylcholine (DOPC) was a product of Avanti Polar Lipids (Birmingham, AL). *N*-(6-((Biotinoyl)amino)hexanoyl)-dipalmitoyl-L-α-phosphatidylethanolamine (B-X-DHPE) was a product of Molecular Probes (Eugene, OR).

Two-dimensional streptavidin crystals were grown on biotinylated phospholipid monolayers in teflon wells using a procedure similar to that described by Kubalek et al. (1991). Twelve microliters of Tris buffer (150 mM NaCl, 50 mM Tris, pH 7) containing 0.20 mg/ml of streptavidin was deposited in a well. Then 1 μl of a 0.25 mg/ml chloroform solution of DOPC and B-X-DHPE, at a ratio of 4:1, was spread on the surface of the protein solution. The crystallization wells were placed in a humid chamber and kept at room temperature for 15 min. A carbon-coated perforated grid (Fukami and Adachi, 1965) was placed on the surface of each well for approximately 30 s. It was withdrawn and the excess liquid was blotted with filter paper. The specimen was preserved in vitreous ice by rapidly plunging the grid into liquid ethane. The frozen, hydrated specimens were transferred to a Gatan cryoholder (model 626; Gatan, Inc.) and kept at −160°C throughout all data collection.

Electron cryomicroscopy

Electron diffraction patterns were recorded on Kodak SO-163 film at 100 kV in a JEOL1200 microscope using a 50 μm condenser aperture and a nominal camera length of 200 cm, without selective aperture. The illuminated area at the specimen contained approximately 240,000 unit cells. The electron dose was 1 electron/Å^2 as measured from a precalibrated picoammeter (model 480 Digital picoammeter; Keithley Instruments, Cleveland, OH) connected to the fluorescent screen of the microscope.

Received for publication 14 July 1995 and in final form 2 October 1995.

Address reprint requests to Dr. Wah Chiu, Baylor College of Medicine, One Baylor Plaza, Houston, TX 77030. Tel.: 713-798-6985; Fax: 713-796-9438; E-mail: wah@bcm.tmc.edu.

The present address of Dr. Sakar is Department of Pharmacology, Health Sciences Center, Box 448, University of Virginia, Charlottesville, VA 22908.

0006-3495/96/01/57/12 $2.00

Electron images were recorded at 400 kV in a JEOL4000 microscope using flood beam illumination and low-dose procedures, similar to those of Jeng and Chiu (1983). The grids were scanned in defocused diffraction mode in search for areas likely to contain crystals. When one such area was found, the diffraction spot was focused and a selective area aperture was inserted. If low-resolution diffraction spots were visible on the fluorescent screen, imaging of that crystal was attempted. Focusing was facilitated by the use of a slow-scan 1024 × 1024 charge-coupled device camera (Gatan, Inc.; Brink and Chiu, 1994). Before each exposure on film, a 512 × 512 pixel image of an adjacent area of the carbon net was recorded and Fourier transformed on line using a DigitalMicrograph (Gatan) (Krivanek and Mooney, 1993; Mooney et al., 1990) to obtain an estimate of the defocus from the contrast transfer function (CTF) ring pattern. Then the objective lens was set to the desired focus and the deflector coils were shifted back on axis using the microscope's user functions (Brink and Chiu, 1991). Images were recorded at a nominal magnification of 40,000× on Kodak SO-163 film with a dose of 8 electrons/Å^2 at the specimen.

All photographic films were developed in Kodak D19 developer for 12 min at 20°C and fixed in Kodak fixer for 10 min.

Data processing

Processing of electron diffraction patterns was done according to the method of Baldwin and Henderson (1984). Crystallographic R-factors were computed as

$$R = \frac{\sum |I_1 - I_2|}{\sum |I_1 + I_2|}$$

where I_1 and I_2 are the intensities of symmetry-related reflections. Friedel symmetry and mirror symmetry about the a^* and b^* axes of the reciprocal lattice were evaluated in this way.

Image processing was done with the aid of the graphic environment of SPECTRA (Schmid et al., 1993) using the Fourier averaging approach (Henderson et al., 1986). Image areas showing sharp optical diffraction spots at a resolution of 4 to 5 Å were digitized in arrays containing approximately 970 unit cells. The scanning step size at the specimen was 1.28 Å. A total of 22 image arrays from six different micrographs were processed. Unbending was applied to correct in-plane lattice distortions for each of the image arrays (Henderson et al., 1986). A reference area 1.5 times the area of a single unit cell was used to search by cross-correlation for the positions of all unit cells in the image and to compute their displacements from the perfect lattice.

A first approximation to the effective defocus was determined from the maximum and minimum positions of the CTF rings (Thon, 1971) when visible. To enhance the visibility of the CTF rings, the amplitudes of the Fourier transforms of many arrays from the local image area in a single micrograph were summed up (Zhou et al., 1995). In Fourier transforms where no CTF rings were visible even after this enhancement, we obtained an initial guess of the defocus and astigmatism parameters by comparing their phases with the CTF-corrected ones from images where Thon rings were visible. In a second step, we refined the CTF parameters of each film against all others by minimizing their merging phases residuals (Bullough and Henderson, 1990), as described below.

We used the program ORIGTILT (MRC, Cambridge, England) to compute phase residuals and beam-tilt corrections among 22 image arrays (Henderson et al., 1986). No symmetry was assumed at this stage. Initially, only two image arrays were compared, one of them with visible CTF rings to about 4 Å resolution. A search for the other image's defocus in two orthogonal directions, Δz_1, Δz_2, and the angle of astigmatism θ with respect to the a^* axis was performed by letting one parameter vary at a time. The phases were flipped by 180° in the appropriate ranges defined by the CTF, using the program CTFAPPLY (based on the MRC code). A coarse defocus search (increments of 200 Å, usually between −0.5 and 0.5 μm) was followed by a finer search with increasingly smaller increments (in some instances down to a 10 Å step). Phase residuals for reflections with IQ ≤ 4 in 12 resolution shells were used for this determination. Parameters that lowered the phase residuals in most or all resolution ranges were kept for the next refinement cycle. One image at a time was added to the merging set and the procedure was repeated until the full set had been merged. Then, each CTF parameter from each image was refined against the full set. At this stage we performed a selection of image arrays by excluding those whose contribution resulted in a deterioration of the phase residuals, rather than an improvement, generally because the phase residual in some resolution ranges could not be brought below 45°. The order of merging was also varied, and only the ones giving the lowest phase residual were chosen. Finally, the refinement was repeated on all selected image arrays, this time using all reflections with IQ ≤ 5.

The final phase shifts after refinement were applied to all reflections with IQ ≤ 8. Figures of merit (FOMs) were computed according to the method of Henderson et al. (1986), using the program AVRGAMPHS (Henderson, 1992b). In addition, the phases from the combined structure factors were evaluated for the presence of twofold rotation axes in the plane and perpendicular to the plane of the crystal.

Generation of 3 Å projection map

A projection map was synthesized by combining the amplitudes (F_{obs}) from an electron diffraction pattern with the merged phases (α_{obs}) from the images. The amplitudes were weighted by the corresponding figure of merit before combination. *cmm* symmetry (see Results) was enforced.

To evaluate the degree of recoverable information from images alone, a Wilson scaling was done between electron diffraction and image amplitudes to estimate a B-factor for the decay of image amplitudes. Projection maps were synthesized with both amplitudes and phases from images, with and without compensation for that B-factor.

Interpretation of the projection map

The atomic coordinates of the streptavidin-biotin complex (Weber et al., 1989) were obtained from the Brookhaven Protein Data Bank. Visualization of the atomic model was done using the program CHAIN (Sack, 1991). A tetramer was generated by applying the known 222 point group symmetry of the molecule (Weber et al., 1989). It was projected along each of the three dyad axes to identify the view in the projection map.

The crystallographic package X-PLOR (Brünger, 1992a) was used to generate an atomic model of streptavidin. Topology and energy parameters for biotin were generated in X-PLOR, using the high-resolution crystal structure of biotin (DeTitta et al., 1976).

With the computed crystal parameters of the streptavidin monolayer crystals, a model crystal was generated and oriented with respect to the electron beam view. The repeat in the z direction was simply a stack of monolayer crystals. Tabulated atomic scattering factors for electrons (Ibers and Hamilton, 1974b) were fitted with a sum of four Gaussian plus a constant for the elements C, N, O, S, and H. The resulting fitting functions were used in the computation of structure factors in X-PLOR. A central section of the 3-dimensional (3-D) diffraction pattern was computed and its amplitudes compared to the experimental electron diffraction amplitudes. R-values were computed according to the formula

$$R = \frac{\sum ||F_{obs}| - k|F_{calc}||}{\sum |F_{obs}|}$$

Phase extension to 2.5 Å

Given that the electron diffraction amplitudes extend to a higher resolution than the image phases (see Results), we refined the atomic model of streptavidin against those amplitudes to extend the resolution of the map. The refinement sequence was 1) rigid body, 2) overall B-factor, and 3) individual atomic coordinates and solvent flattening. The cross-validation criterion, R-free value (Brünger, 1992b), was used to prevent overfitting of the data.

RESULTS

Electron diffraction

Fig. 1 shows one of the best electron diffraction patterns from a streptavidin monolayer crystal embedded in vitreous ice extending to 2.5 Å resolution. The diffuse background scattering has been subtracted. The center of the pattern, which is replaced by a disk, is saturated by the direct electron beam and the low angle inelastic scattering. Diffraction patterns of streptavidin crystals on lipid monolayers are not always of the same quality as the one shown in Fig. 1. They frequently show split reflections arising from the presence of multiple lattices in the field covered by the electron beam, or blurring possibly due to long-range distortions of the crystals. The percentage success in getting diffraction patterns that did not suffer from those defects was less than 10%.

The overall Friedel R_{sym} factor was 0.09 for 638 pairs of reflections between 20 and 2.5 Å in the pattern shown in Fig. 1. The distribution of reflections suggests mirror symmetry about a^* and b^*, and systematic absences for indices $h + k = 2n + 1$. This is consistent with a centered plane group, like *cm* or *cmm* (Ibers and Hamilton, 1974a). The R_{sym} factors for reflections related by those putative mirror axes was 0.20, about twice as large as the Friedel R_{sym} factor. This could be due to a slight tilt of the crystal with respect to the electron beam. In an electron diffraction pattern recorded from a glucose-embedded crystal (not shown), the R_{sym} for the two mirror axes was 0.10 up to 2.5 Å. As will be shown below, *cmm* symmetry is also consistent with the phases extracted from the images.

The pattern in Fig. 1 is characterized by strong intensities between 20 and 10 Å, then a considerable reduction in the diffracting power between 10 and 6 Å, followed by strong intensities between 6 and 3.5 Å. Strong diffracting power along the a^* axis with maxima between 4.5 and 5 Å can be interpreted as indicative of β-sheet structure, the spacing between β-strands being around 4.8 Å (Astbury and Woods, 1933; Brown and Trotter, 1956). From the intensity distribution of the pattern, it is expected that some β-sheets may be aligned roughly parallel to the b axis of the unit cell.

Electron images

Initial attempts to image streptavidin crystals failed frequently as a consequence of beam induced specimen movement. The success rate increased dramatically when a larger beam diameter was used which also imaged part of the carbon support film of the perforated grid. Fig. 2 shows a digitized image array from a 400 kV electron micrograph of an ice-embedded streptavidin crystal across a hole without carbon support film. The area contains approximately 970 unit cells. The defocus value of this image was determined to be about 0.3 μm. Therefore, it exhibits very little contrast. However, the analysis of the Fourier transform of this image revealed components with high signal-to-noise (s/n) beyond 4 Å resolution. Fig. 3 displays the s/n ratio of the reflections extracted from the amplitude peaks on the reciprocal lattice relative to its local background. The procedure was carried out using the graphic display of the program SPECTRA (Schmid et al., 1993), and the programs LATREF and MNBOX (MRC). In the figure, the conven-

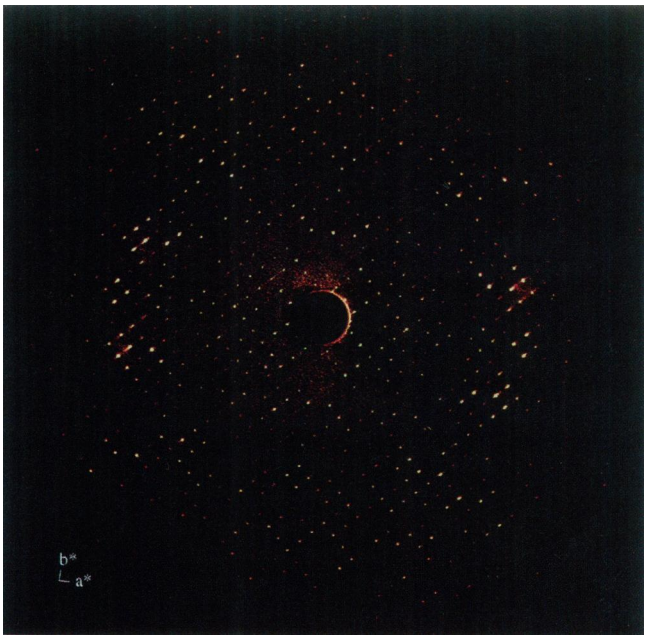

FIGURE 1 Electron diffraction pattern of ice-embedded streptavidin crystal grown on a biotinylated phospholipid monolayer. Unit cell parameters are a = 82.3 Å, b = 82.3 Å, γ = 90.0°. Highest resolution reflections corresponding to a Bragg spacing of 2.5 Å are detectable.

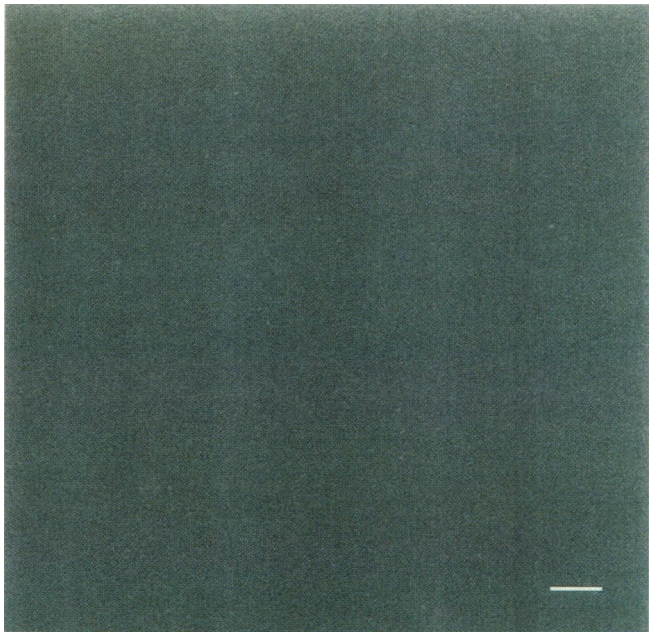

FIGURE 2 Digitized 400 kV electron image array of an ice-embedded streptavidin crystal grown on a biotinylated phospholipid monolayer. The area contains approximately 970 unit cells. The image contrast is very low, partly because the defocus was <0.5 μm. The scale bar represents 200 Å.

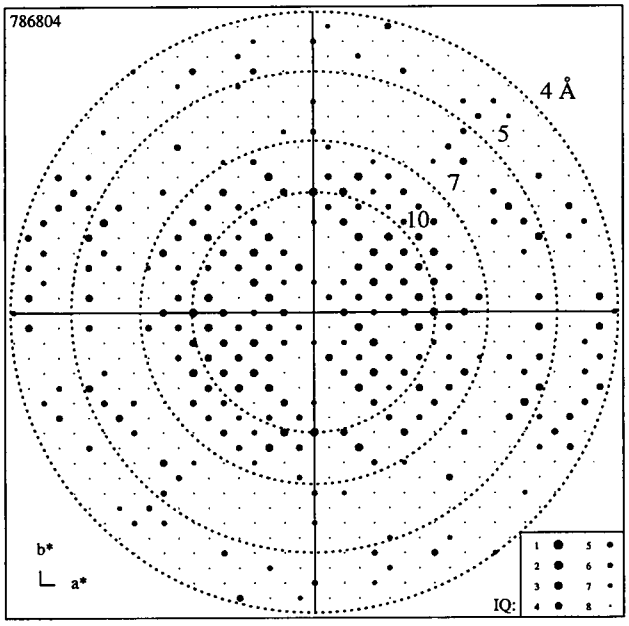

FIGURE 3 Schematic representation of the Fourier components of the image shown in Fig. 2. The sizes of the circles are related to the signal-to-noise ratio (s/n), according to their IQ index (see text). Terms with IQ $\leq$ 4 have a s/n ratio $\geq$ 2.

tional IQ scale (Henderson et al., 1986) is used. As a guideline, IQ $\leq$ 4 is equivalent to s/n $>$ 2.0, IQ $\leq$ 5 is equivalent to s/n $>$ 1.6, and IQ $\leq$ 8 is equivalent to s/n $>$ 1.0. The full processing, including unbending and corrections for the microscope's contrast transfer function (CTF), was carried out on a set of 22 image arrays from six negatives recorded from different crystal preparations. After unbending, a typical increase in the overall s/n ratio was 35%.

CTF determination and merging of image arrays

CTF rings were visible in some images from streptavidin, because the illuminated field included part of the carbon net supporting the specimen. The visibility of those CTF rings was enhanced after summing up the amplitudes of the Fourier transforms of many arrays from the local image area. However, other images did not show CTF rings in their transforms even after enhancement. An initial guess of their defocus values was arrived at by comparing their phases with the corrected ones from those in which the CTF rings were visible. The use of electron diffraction amplitudes to refine the CTF parameters resulted in a set of phases with an overall merging phase residual of 25.5° for reflections with IQ $\leq$ 4 from 22 image arrays to 3.0 Å resolution. However, phase residuals at resolutions beyond 5 Å became unacceptably high, with some being as high as 90°. The refinement of the CTF parameters based on phase information alone (with starting values derived from Thon rings and phase comparisons, as described in Materials and Methods) eventually resulted in a coherent set of phases to 3.0 Å resolution, with an overall merging phase residual of 18.3° for all reflections with IQ $\leq$ 5 from five final image arrays extracted from four films. Beam tilt adjustments ranged from −2.0 to 3.4 milliradians. The CTF parameters for the four films included in the final merging set are in Table 1 and the merging phase residuals by resolution zones appear in Table 2.

The structure factors were combined according to the method of Henderson et al. (1986). Figures of merit (FOMs) were derived from phase probability distributions according to the method of Henderson (1986). The mean FOM was 0.67 for reflections with IQ $\leq$ 8 and 0.97 for reflections with IQ $\leq$ 5. Mirror phase residuals about the a^* and b^* axes, respectively, were 31° and 27° for all merged structure factors (18° and 15° for structure factors with FOM $\geq$ 0.76). The phase residual for a twofold symmetry axis perpendicular to the crystal plane was 30° for all combined structure factors (24° for structure factors with FOM $\geq$ 0.76). The low mirror and twofold phase residuals, particularly for reflections with high FOM, suggest that the projection map has *cmm* symmetry. Assuming a single protein layer (which is strongly supported by the interpretation of the map with the atomic model; see below), this projection symmetry is consistent with the two-sided plane group *c222* (Holser, 1958).

Combination of amplitudes and phases

Image phases were combined with the electron diffraction amplitudes to generate a structure factor set with 217 unique terms to 3.0 Å resolution. They were enforced according to plane group *cmm*. The amplitudes were weighted by the corresponding FOM before combination. Fig. 4 shows a histogram of the resulting structure factors as a function of their FOM. To evaluate the FOM as a parameter for measuring the reliability of the data, we generated another set of structure factors from the forbidden reflections ($h + k = 2n + 1$) of the same five image arrays. Such set is expected to represent the distribution of noise in the images. The frequency of reflections with 1.00 $\geq$ FOM $\geq$ 0.95 was clearly greater in the data set than in the noise set. For reflections with 0.95 $\geq$ FOM $\geq$ 0.90 the frequency of reflections in the data was marginally greater than in the noise. The frequency of structure factors with FOM $<$ 0.90 was not greater than that of the noise structure factors. Table 2 shows the distribution of reflections with FOM $\geq$ 0.90 by resolution zones, and Fig. 5 shows the FOM for all reflections after merging from the four images. The size of the circles is a function of

TABLE 1 Defocus and astigmatism values for four films

Image ID	Dz_1 (Å)	Dz_2 (Å)	θ(°)
7816	−2725	−4060	−38
7887	−5270	−4600	−2
7888	3987	4400	57
7845	−3905	−5545	155

TABLE 2 Phase reliability statistics by resolution zones

Resolution range (Å)	Merging phase residuals (IQ ≤ 5)	Mean figure of merit	Frequency of phases with FOM ≥ 0.90		Fraction of phases identical to model	Completeness
			Data*	Noise‡		
20.0–10.4	13.3	0.938	0.92	0.07	0.86	1.00
10.4–7.3	26.8	0.878	0.82	0.04	0.88	0.72
7.3–6.0	12.3	0.777	0.71	0.07	0.82	0.73
6.0–5.2	19.8	0.704	0.65	0.09	0.78	0.96
5.2–4.6	41.2	0.697	0.48	0.04	0.90	0.78
4.6–4.2	12.3	0.790	0.67	0.00	0.86	0.86
4.2–3.9	30.6	0.529	0.58	0.05	0.89	0.81
3.9–3.7	31.9	0.554	0.69	0.02	0.81	0.85
3.7–3.5	—	0.488	0.40	0.07	0.60	0.67
3.5–3.3	31.3	0.491	0.11	0.02	0.93	0.54
3.3–3.1	1.1	0.495	0.49	0.04	0.62	0.62
3.1–3.0	—	0.533	0.20	0.00	0.20	0.26
Overall	18.3	0.657	0.60	0.04	0.80	0.74

*Final structure factor set used in the generation of the projection map.
‡Set extracted from the forbidden reflections of the image arrays.

the electron diffraction intensities. Filled circles correspond to phases with FOM ≥ 0.90.

Projection map

A projection map was synthesized with amplitudes from electron diffraction and phases from images including data to 3.0 Å resolution. In Fig. 6, the densities in the map are displayed using gray levels. High densities are white. The area shown corresponds to two unit cells. We used the atomic model of a streptavidin tetramer to interpret the densities in the map. First we noted that the 222 point group symmetric tetramer (Weber et al., 1989; Hendrickson et al., 1989) could give rise to *cmm* symmetry in projection along each of the three mutually perpendicular twofold axes. Such axes were conventionally designated as P, Q, R by Hendrickson et al. (1989). Images along those directions were simulated using X-PLOR and compared visually to our experimental map. In that manner, the direction of view was unambiguously determined to be along the R dyad axis. In the figure, the atomic backbone of one streptavidin tetramer is overlaid on the projection map. The Q and P dyads coincide with the horizontal and vertical mirror lines of the projection map, respectively, whereas the R dyad is perpendicular to the projection plane.

Fig. 7 shows one unit cell with the atomic model overlaid (for clarity, two protomers have been omitted). Each subunit is an eight-stranded β-barrel (Weber et al., 1989; Hendrickson et al., 1989). Along this view, the densities of four β-strands from two Q dyad-related subunits align at the level of the projected Q dyad (labels in Fig. 7 indicate the particular strands involved, according to the polypeptide sequence). Three of them (β-strands 6, 7 and 8) actually overlap with the Q dyad-related ones, giving rise to strong density peaks. The loop between β-strands 5 and 6 also shows considerable overlap, both within a single subunit and between the two subunits, and coincides with a high density peak. Below that peak, part of a single strand (β-strand 5) is visible. The central densities from β-strands 8 are split, and give rise to the four peaks in the middle of the map. Each peak is produced by three overlapping residues, two from one subunit (Leu 124 and Val 125), and one from the subunit related by the Q dyad (Thr 123). The very strong peak along the vertical (projected P dyad), 10 Å away from the center of the molecule, coincides with the overlap of six residues from all four subunits, including the stacked aromatic rings from two P dyad-related histidine (His 127), with a closest contact of 3.1 Å in the atomic model, as measured from the atomic coordinates (Weber et al., 1989), using the program CHAIN (Sack, 1991). The other overlapping residues at that peak are two asparagines and two alanines (Asp 118, Ala 119, and the P dyad-related mates). The total mass contributed by those six residues is about 752.

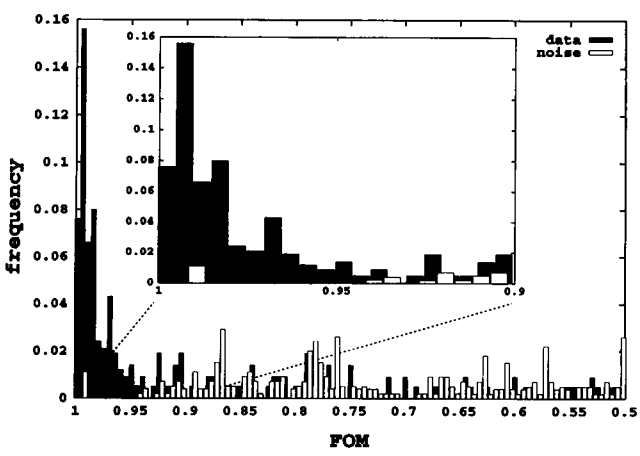

FIGURE 4 Figure of merit (FOM) histograms for combined data and noise from about 6000 unit cells, up to a resolution of 3 Å.

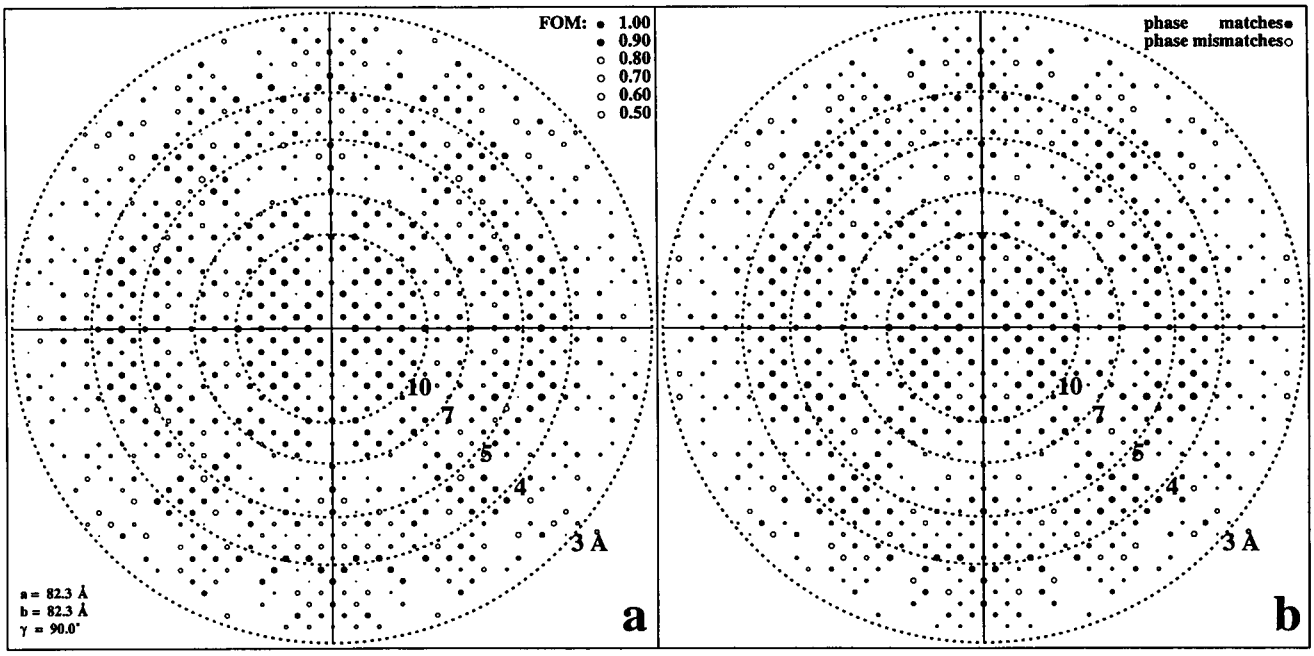

FIGURE 5 (*a*) Schematic representation of the set of combined structure factors in the reciprocal plane to 3 Å resolution. The size of the circles is a function of the electron diffraction amplitude. Filled circles correspond to reflections with FOM ≥ 0.90 in their merged phases; open circles represent those with FOM between 0.9 and 0.5. (*b*) Distribution of phase identities between cryomicroscopy and model in the reciprocal plane to 3 Å resolution. Because of the *cmm* symmetry of the projection, the phases could only be either 0° or 180°. Therefore, the experimental phases either match the model exactly (*filled circles*) or are 180° degrees apart (*open circles*). As in *a*, the size of circles is a function of the corresponding electron diffraction amplitudes.

An interesting region occurs close to the inter-tetramer contact. The only overlaps around this area are within single subunits. Fig. 8 shows a detailed view of that region. The densities from electron cryomicroscopy data are now displayed as contour levels. The contour lines are separated by intervals of 0.5 σ starting from the mean density of the map and ending at 3.0 σ. Levels above 1.0 σ are colored blue. The localized strong peak at the center of the display coincides with two overlapping aromatic side chains, one from Tyr 96 and one from Trp 21, this last one seen almost edge-on. The two side chains are relatively close to each other in space (closest contact = 3.8 Å). In addition to those side chains, the only other overlapping residue is Thr 28. The total mass contributing to that peak is about 504 Da. The boundary between two tetramers is also visible in that figure. It includes 11 residues from each tetramer with a mean distance of 4.0 Å.

To obtain a quantitative measure of the similarity between the projected reconstruction and the atomic model, we computed structure factors from the atomic model using X-PLOR. They were compared to the amplitudes and phases from electron cryomicroscopy. The R-factor for amplitudes between 20 and 2.5 Å was found to be 0.39. Eighty percent of the phases between 20 to 3.0 Å were identical in model and cryomicroscopy (Table 2). The distribution of phase identities in the reciprocal lattice is plotted in Fig. 5 *b*.

Maps with amplitudes from images

The projection maps shown in Figs. 6, 7, and 8 were derived exclusively from electron cryomicroscopy data, without the aid of the atomic model information. The atomic model has been used only for comparison and interpretation. To evaluate the degree of recoverable information from images alone, a Wilson scaling was done between electron diffraction and image amplitudes to estimate a B-factor for decay of the image amplitudes. The B-factor then obtained was 116 Å^2. In Fig. 9, a projection map obtained with image amplitudes alone is compared to one in which the image amplitudes have been corrected for that resolution-dependent decay. Both maps are compared to the projection map generated with electron diffraction amplitudes. The three maps include data to 3.0 Å resolution.

Phase extension

The data included in the map extend to 3.0 Å, but as stated before, there is measurable intensity in the diffraction patterns up to 2.5 Å. The atomic model was refined against the electron diffraction amplitudes, in an attempt to extend the resolution of the map to 2.5 Å. The course of the refinement is shown in Table 3 in terms of overall *R*-value and *R*-free value. The initial and final *R*-factors are shown in various resolution zones in Table 4. Deviations of the refined model from ideality appear in that Table 5. The rms deviation from

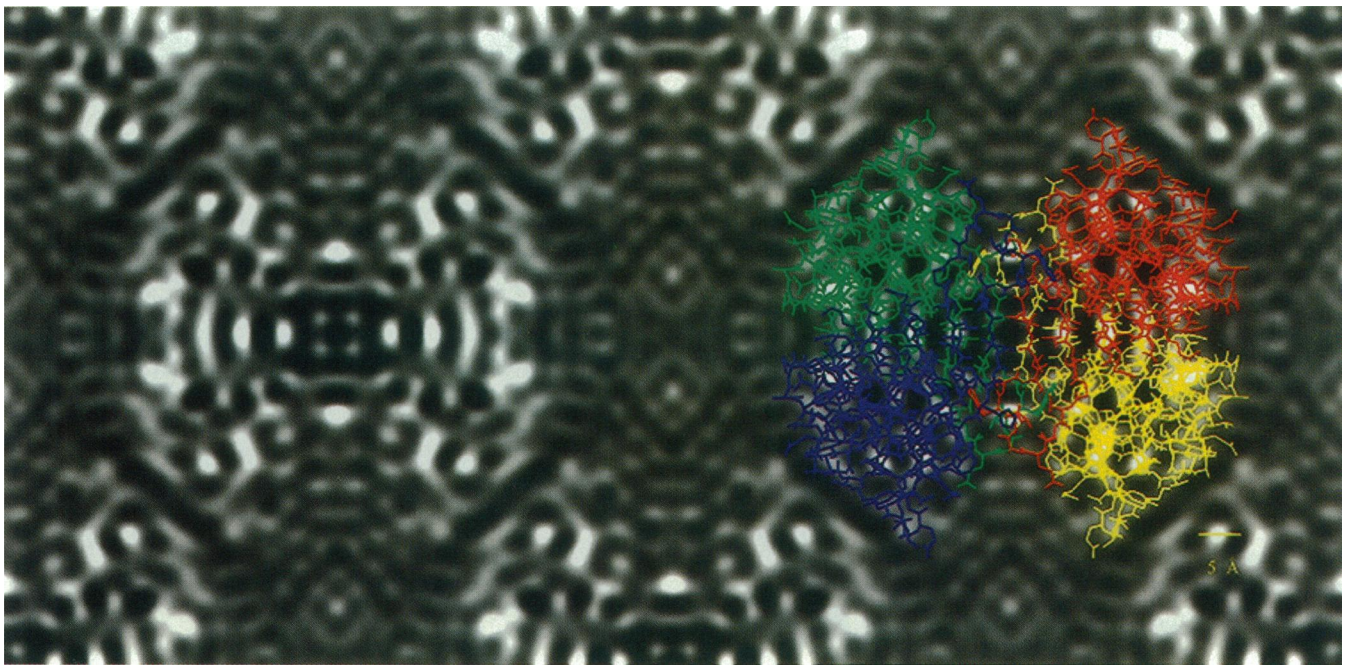

FIGURE 6 3 Å projection map of streptavidin by electron crystallography. Amplitudes were from electron diffraction; phases were from electron imaging. Two unit cells are shown, each with a tetramer at the center and portions of adjacent ones at the corners. The atomic model of the molecule, as obtained from the Brookhaven Protein Data Bank (Weber et al., 1989), is overlaid on one of the tetramers. Protomers within the tetramer are displayed with different colors. The Q and P dyads coincide with the horizontal and vertical mirror lines of the projection map, respectively, whereas the R dyad is perpendicular to the projection plane.

starting model was 0.20 Å. The average B-factor was 12.4 $Å^2$. Fig. 10 shows a detail of the projection map to 2.5 Å resolution, where there is little overlap between different subunits of the tetramer. The refined atomic model is overlaid.

DISCUSSION

Crystal quality

The remarkable ease of producing 2-D streptavidin crystals on phospholipid monolayers contrasts with the relatively low frequency of crystals of good quality for electron diffraction purposes. As stated above, only a very small fraction were collected in ice that would show sharp, high-resolution reflections arising from a single crystalline lattice, like the one shown in Fig. 1. That pattern showed apparent mirror symmetry. However, the computed *R*-factors for the mirror lines (0.20) were relatively high, as compared to the *R*-Friedel (0.09). The information from image phases, as well as from some electron diffraction patterns from glucose-embedded specimens, strongly suggested *cmm* symmetry. Therefore the small deviations in the ice-embedded sample were most likely due to slight tilt. The inaccuracy introduced by considering the amplitudes as derived from an untilted crystal were inevitably carried over to subsequent stages of the analysis. Nevertheless, the most important question in this study was whether the phases could be retrieved reliably from electron images. It is known from simulations with x-ray crystallographic data that density maps with correct phases and inaccurate amplitudes are interpretable in terms of atomic structures, whereas maps with accurate amplitudes but incorrect phases are completely uninterpretable (Cantor and Schimmel, 1980). Therefore, to a first approximation, it was expected that some interpretable densities could be obtained in spite of the questionable amplitudes if the correct phases were retrieved.

Electron images

Attempts to record electron images from streptavidin crystals consistently failed when using a small diameter (1000 to 2000 Å) for spot-scan imaging. When searching for crystals at low magnification, it was noticed that the beam could change in diameter drastically as it moved from a carbon film area to the middle of a hole where it stopped making contact with the carbon film. This phenomenon probably indicated charging of the specimen, as has been observed using various specimens, including streptavidin embedded in glucose (Brink et al., 1994). To avoid this problem we tried to include part of the carbon film in all pictures. Therefore, we used a beam diameter of 1.6 μm. This indeed resulted in a higher success rate. All images included in this study were recorded in this way.

Most image arrays processed did not have major lattice distortions. However, some increase in s/n ratio was obtained in each of them after unbending. Interestingly, the

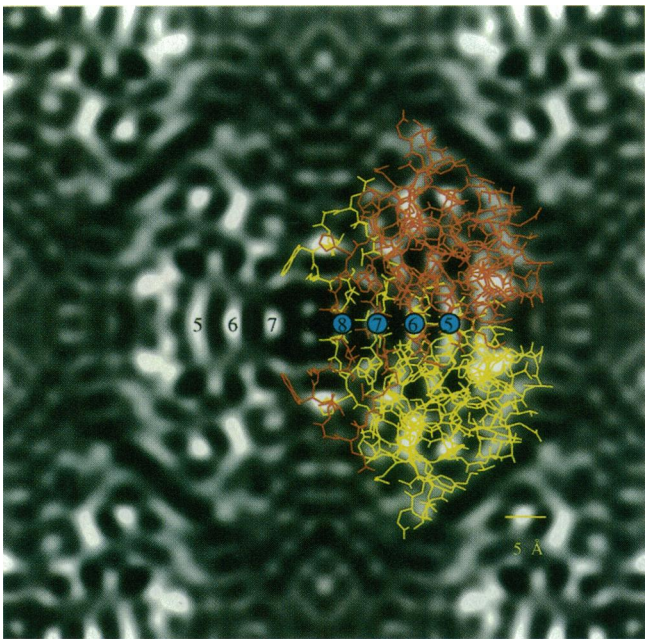

FIGURE 7 3 Å projection map of streptavidin by electron crystallography. One unit cell is shown with PDB atomic model overlaid (two protomers are omitted for clarity). The densities along the horizontal mirror line of the tetramer (Q dyad in projection) arise from the overlap of segments of four β-strands of one protomer with the Q dyad related ones from the adjacent protomer (in the figure numbered according to the polypeptide sequence).

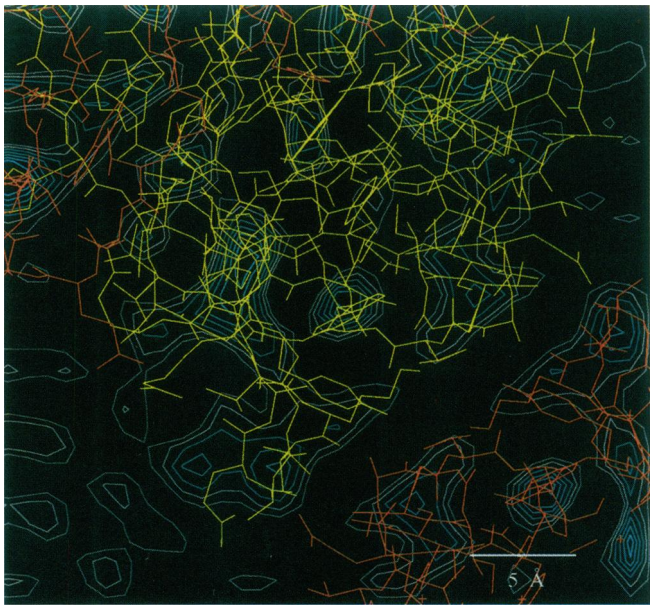

FIGURE 8 Detailed view of a region with densities from one subunit only. The strong peak close to the center of the figure coincides with the overlapping aromatic side chains of Tyr96 and Trp21. The boundary between adjacent tetramers is also visible here. It includes 11 residues from each side, and the mean distance between tetramers is 4.0 Å. Contour levels (in σ units) in both *a* and *b*: blue: 3.0, 2.5, 2.0, 1.5, 1.0; gray: 0.5, 0.1.

search for cross-correlation peaks was more successful when using a reference area smaller than conventionally used in such procedures. Usually, a patch with an area equivalent to 1% of the total area is cross-correlated with the filtered image of the array. In this study, the reference area was 0.16% of the total area, equivalent to 1.5 unit cells.

CTF refinement and merging

Whereas some images showed CTF rings that enabled the initial determination of defocus and astigmatism values, others did not show such rings. An initial guess of their values was arrived at by a comparison of their phases with the corrected ones from one in which the CTF rings were visible. However, the use of electron diffraction amplitudes to refine the CTF parameters did not result in a satisfactory set of coherent phases. The reason could be that, as already discussed above, the electron diffraction amplitudes carried a deviation from mirror symmetry (R_{sym} = 0.20) that was twice as large as the counting statistics inaccuracy ($R_{Friedel}$ = 0.09). Therefore, we decided to rely on the phases to conduct a refinement of the CTF, under the assumption that a correct CTF determination would lead to a minimal phase residual among the image arrays compared. The final overall phase residual of 18.3° for all reflections with IQ $\leq$ 5 indeed suggests that the CTF corrected phases are coherent (for comparison, the phase residual without CTF correction was 58°).

The improvement in merging phase residuals after CTF refinement was paralleled by an improvement in symmetry phase residuals consistent with *cmm* projection symmetry. This brings up an interesting point, because a number of studies indicate that each tetramer with a 222 symmetry should have two occupied biotin binding sites interacting with the monolayer and two empty ones facing away from the monolayer (Darst et al., 1991; Hemming et al., 1995; Herron et al., 1992; Müller et al., 1993), which allows for *p*2 symmetry, but strictly not *c*222 symmetry. However, our data were merged under the *p*1 assumption, and the *cmm* symmetry was deduced exclusively from the low phase residuals about the reciprocal axes a^* and b^*. Under the *cmm* symmetry, all four sites are equivalent in projection. Therefore, our current projection data are not sufficient to detect the structural difference, if any, among the biotin binding sites.

Reliability of phases

The figure of merit (FOM) has been used to evaluate the reliability of phase determinations in electron images (Henderson et al., 1986; Hayward and Stroud, 1981; Brillinger et al., 1990; Bullough and Henderson, 1990). In this study it was found empirically that for FOM $<$ 0.90 the distribution of FOM values in the data set is not distinguishable from a distribution of FOM values extracted from noise. For example, a structure factor with 0.70 $<$ FOM $\leq$ 0.80 is as likely to occur in a combination of true structure factors as in a combination of noise structure factors. Only

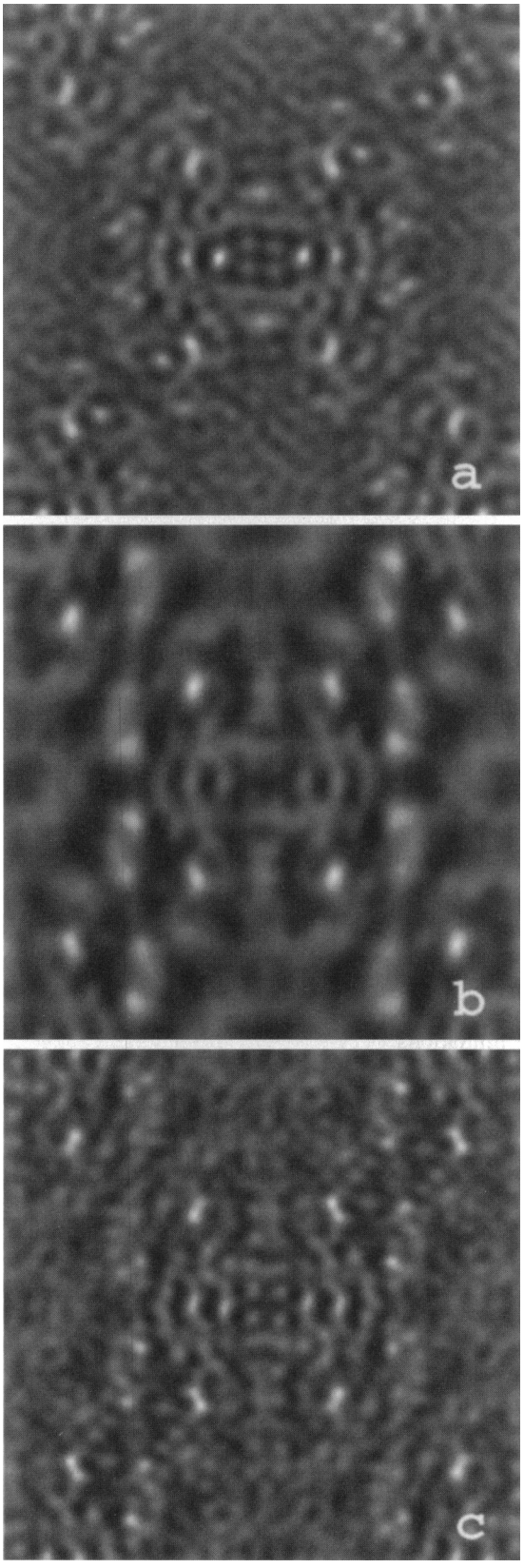

FIGURE 9 (*a*) Projection map with electron image amplitudes and phases. (*b*) Map using same data as in *a* but with a correction for a B-factor of 116 Å^2. (*c*) Projection map using electron diffraction amplitudes and electron image phases.

TABLE 3 *R*-free and *R*-factor values at different stages of the refinement of the atomic model against the electron diffraction amplitudes

	Initial (PDB file)	Rigid body*	Overall B-factor‡	*x,y,z* and solvent§
R-free‖	0.48	0.48	0.43	0.39
R-factor¶	0.38	0.37	0.37	0.18

*Eulerian angles of rotation (°): 0.02, 1.02, 1.73; translation along *x,y,z* (Å): −0.02, −0.05, 0.01.
‡$B = -10.42$ Å^2.
§Solvent correction: $k = 0.03$, $B = 100$ Å^2; solvent content in protein layer: 48%.
‖Test (cross-validation) set: random 10% of the reflections.
¶Working set: 90% of the reflections.

values with FOM ≥ 0.90 occur with a higher frequency in the data set. Although the result cannot be directly extrapolated to other data sets, it suggests that one should be cautious about reflections with FOM < 0.90. The percentage of reflections with FOM ≥ 0.90 in the streptavidin data set was 60%. Fig. 5 clearly indicates that those high FOMs are predominantly associated with strong intensities. Moreover, Table 2 shows that the percentage is high at low resolution and decreases at high resolution.

Projection maps and their reliability

As mentioned earlier, one of the motivations for carrying out this study was the availability of an atomic model of streptavidin derived from x-ray crystallography (Weber et al., 1989; Hendrickson et al., 1989), so that we could evaluate the electron crystallographic method for 2-D crystals grown on lipid monolayers. Figs. 6, 7, and 8 show qualitatively that the most outstanding features of the projection map can be interpreted by direct comparison with the atomic backbone of streptavidin. Most importantly, the expected densities for β-sheets were found along the horizontal mirror axes and correspond to overlapping β-strands, at a region of extensive contact between Q dyad-related subunits. On the other hand, some regions of the map, especially near the edge of the molecule, had poorly defined densities. They correspond mainly to regions of the molecule with high temperature factors, according to the atomic model (Weber et al., 1989).

Another way to verify our map is to examine the structure factors relative to those from the model. A quantitative comparison of the amplitudes of the structure factors between model and cryomicroscopy yielded an *R*-factor of 0.39. Such high *R*-factors may reflect some of the inaccuracies in the electron diffraction amplitudes mentioned earlier. But it may also be a reflection of slight conformational differences between streptavidin in a 3-D crystal environment and streptavidin adsorbed to a phospholipid monolayer. The phases are 80% identical between model and microscopy up to 3.0 Å resolution (Table 2). In fact, a closer inspection by resolution zones shows that the percentage identity is greater in some ranges, for example 90% between

TABLE 4 Initial and final *R*-factors by resolution zones

Resolution range (Å)	Initial (PDB file)		Final		
	R-free*	*R*-factor‡	*R*-free*	*R*-factor‡	Completeness
20.0–5.7	0.42	0.44	0.25	0.23	0.79
5.7–4.5	0.22	0.33	0.24	0.13	0.94
4.5–4.0	0.61	0.33	0.52	0.13	0.83
4.0–3.6	0.21	0.35	0.23	0.14	0.77
3.6–3.3	0.87	0.32	0.72	0.16	0.62
3.3–3.2	0.46	0.49	0.44	0.26	0.73
3.2–3.0	0.82	0.46	0.74	0.19	0.31
3.0–2.9	0.60	0.48	0.52	0.19	0.70
2.9–2.8	—	0.42	—	0.29	0.48
2.8–2.7	—	0.45	—	0.16	0.33
2.7–2.6	0.49	0.33	0.45	0.21	0.48
2.6–2.5	—	0.34	—	0.25	0.57
Overall	0.48	0.38	0.39	0.18	0.67

*Test (cross-validation) set: random 10% of the reflections.
‡Working set: 90% of the reflections.

5.2 and 4.6 Å (Table 2). There is a drastic decrease in identity observed between 3.1 and 3.0 Å, and the data completeness drops to about 26% at that resolution. The percentage of FOM $\geq$ 0.90 also shows a significant decrease in that range (Table 2). Projection maps generated with various resolution cutoffs showed no apparent gain in structural detail when going from 3.3 to 3.0 Å. For practical purposes, therefore, the effective resolution of the reconstruction would be ~3.3 Å from data derived exclusively from electron diffraction and imaging.

An obvious consideration is how important is it to have electron diffraction data versus electron images alone. Recent studies have shown promising results toward high-resolution structure determination without electron diffraction amplitudes (Unger and Schertler, 1995). In the case of streptavidin, we could not distinguish many features of the projection structure from a reconstruction based on image amplitudes alone. If those amplitudes are multiplied by a compensation factor for the resolution-dependent decay, as in the work by Unger and Schertler (1995), some features become recognizable. However, the noise in our map is also greatly amplified. It is not clear whether one could tell which features are true and which are noise in the absence of the known structure of streptavidin. Our results tend to favor the need of electron diffraction amplitudes for high-resolution structure determination, but it may well be that averaging over a larger image data set could overcome the noise limitations.

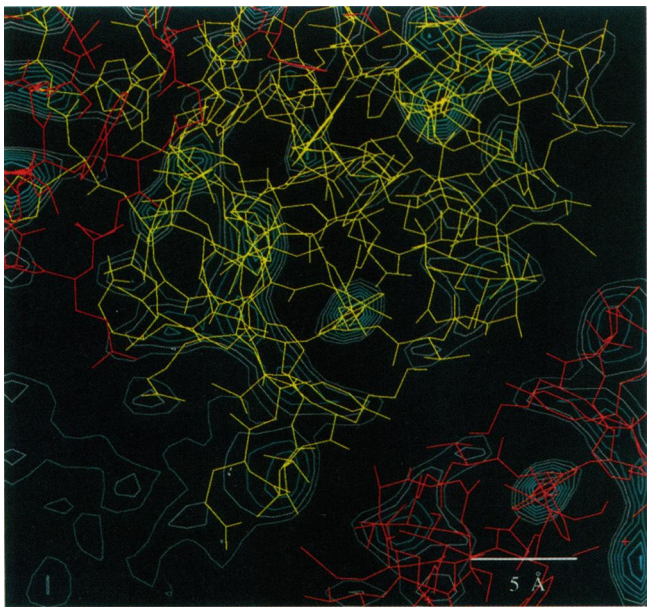

FIGURE 10 Detailed view of projection map after refinement of the atomic model against the electron diffraction amplitudes. Area shown and contour levels are the same as in Fig. 8. The map includes data to 2.5 Å resolution. Notice that the density peaks are sharper and better localized around most of the amino acid chain clusters.

To extend the resolution of the map to the limit of the electron diffraction data, we refined the atomic model of the streptavidin tetramer against the electron diffraction amplitudes to 2.5 Å resolution. Rigid body refinement produced only a small change in the position and orientation of the subunits with respect to each other (Table 3), with marginal drop in the *R*-factor and *R*-free factor. The application of an overall B-factor resulted in a 5% drop of *R*-free factor but no significant drop in *R*-factor. Finally, refinement of individual atomic coordinates and inclusion of bulk solvent resulted in a further 4% drop of *R*-free factor and a 19% drop in *R*-factor. The final *R*-factor of 18% is comparable to values commonly obtained in the refinement of protein structures in x-ray crystallography. The final model has good geometry, as indicated by the bond and angle deviations from ideality in Table 5. The reconstructed projected potential to 2.5 Å shows more and better defined density peaks. The detail shown in Fig. 10 reveals sharper and better localized peaks around most of the amino acid side-chain clusters. The rms deviation of the model from the starting one suggests that the conformation of streptavidin on the monolayer is not appreciably different from that in the 3-D

TABLE 5 rms deviations from ideal (1148 atoms)

Bonds	0.017 Å
Angles	3.5°
Dihedrals	27.4°
Impropers	1.4°

crystal packing. Clearly, a 3-D density map is needed to test this hypothesis and arrive at a precise description of the structure of streptavidin on the monolayer.

Prospects for 3-dimensional structure

One of the goals in the study of streptavidin on a biotinylated phospholipid monolayer is to examine its structure upon binding to a surface with and without the biotin. In the crystal packing, two subunits of the tetrameric streptavidin would be bound to the biotinylated phospholipid monolayer, whereas the other two would be facing the aqueous phase. Based on the present projection data alone, it was not possible to demonstrate such a distinction, because most likely the expected differences are within the experimental error. It may be useful to include data from specimens with biotinylated lipids carrying a heavy atom, for example gold. This could provide a direct experimental tool to answer the question about how many biotin sites are actually occupied on streptavidin on the lipid monolayer. However, visualizing possible conformational changes derived from such partial occupancy of the biotin binding sites should await a full 3-D structural study. Another potential interest in studying the streptavidin crystal on a phospholipid monolayer is to see if there is any ordered lipid, and, if so, to determine its interaction with the proteins. The current analysis did not reveal such features, but it may become possible with three-dimensional data and better resolution. Based on our limited trials, it is difficult to obtain flat enough crystals embedded in ice for the collection of tilted data necessary for 3-D reconstruction. However, using glucose-embedded specimens, we were able to record electron diffraction patterns at a nominal tilt angle of 50° with data to 3 Å (Avila-Sakar, 1995).

CONCLUSION

The present work demonstrates the potential of retrieving reliably near-atomic resolution information from biological macromolecules on phospholipid monolayers by electron crystallography. A 3 Å projection map of streptavidin was generated with amplitudes and phases from electron diffraction and electron images, respectively. The map shows interpretable projection densities in terms of the atomic model of the molecule. This is the first near-atomic projection image of a protein crystallized on phospholipid monolayers. Structural details at the level of secondary structure were identified. Features of the map arising from only a few overlapping amino acid side chains were also identified. Although image data are limited to 3 Å in this study, there is no reason to believe that such limitations could not be overcome by a more exhaustive image data collection to 2.5 Å, the resolution limit of the crystal, as demonstrated by its diffraction pattern. It is conceivable that other proteins could be crystallized with similar techniques and be studied to the same level of resolution.

An interesting prospect for extending the current analysis is the possible future applications of the streptavidin monolayers to solve structures of other biomolecules. In principle there are many proteins of unknown structure that could bind to a preformed streptavidin monolayer via simple or complex linkers. In some cases, such constructs have demonstrated some functionality and are therefore of biotechnological relevance (Herron et al., 1992; Morgan and Taylor, 1992; Müller et al., 1993). One should keep in mind that recognition processes in biology and biotechnology are fundamentally related to the structures involved. For that reason, detailed knowledge of molecular structure is likely to influence our understanding of the function of biological systems, as well as biotechnological devices, such as biosensors. Structural characterization of biological surfaces at the atomic level demands the utilization of numerous modern techniques (Helm et al., 1991; Weisenhorn et al., 1992; Furano and Sasabe, 1993; Haas et al., 1995). Electron crystallography may well become one of the structural tools for high-resolution analysis of macromolecules (Chiu and Schmid, 1993).

We are thankful to Dr. Pat Weber for discussions on the results. We thank Dr. Jaap Brink and Dr. George N. Phillips, Jr., for suggesting the idea of refining the model against the electron diffraction data. We thank Dr. Mike Quillin for help with the crystallographic program X-PLOR. We thank Dr. Michael F. Schmid, Dr. B. V. V. Prasad, Dr. Jaap Brink, Dr. Misha Sherman, and Dr. Elena Orlova for many helpful discussions during analysis of the data and preparation of the manuscript.

This work has been supported by grants from the R. A. Welch Foundation, the W. M. Keck Foundation, NSF BIR9413229, and NCRR of the National Institutes of Health (RR02250).

REFERENCES

Ahlers, M., R. Blankenburg, D. W. Grainger, P. Meller, H. Ringsdorf, and C. Salesse. 1989. Specific recognition and formation of two-dimensional streptavidin domains in monolayers: applications to molecular devices. *Thin Solid Films.* 180:93–99.

Ahlers, M., W. Müller, A. Reichert, H. Ringsdorf, and J. Venzmer. 1990. Specific interactions of proteins with functional lipid monolayers—ways of simulating biomembrane processes. *Angew. Chem. Int. Ed. Engl.* 29:1269–1285.

Astbury, W. T., and H. J. Woods. 1933. X-ray studies of the structure of hair, wool and related fibres. II. The molecular structure and elastic properties of hair keratin. *Philos. Trans. R. Soc. Lond. A* 232:333–394.

Avila-Sakar, A. J. 1995. Electron crystallography of biological macromolecules and complexes. Ph.D. thesis. Baylor College of Medicine, Houston, Texas.

Avila-Sakar, A. J., T. L. Guan, T. Arad, M. F. Schmid, T. W. Loke, A. Yonath, J. Piefke, F. Franceschi, and W. Chiu. 1994. Electron cryomicroscopy of *Bacillus stearothermophilus* 50 S ribosomal subunits crystallized on phospholipid monolayers. *J. Mol. Biol.* 239:689–697.

Baldwin, J. M., and R. Henderson. 1984. Measurement and evaluation of electron diffraction patterns from two-dimensional crystals. *Ultramicroscopy.* 14:319–336.

Bayer, E. A., and M. Wilchek, editors. 1990. Avidin-biotin technology. *Methods Enzymol.* 184.

Blankenburg, R., P. Meller, H. Ringsdorf, and C. Salesse. 1989. Interaction between biotin lipids and streptavidin in monolayers: formation of oriented two-dimensional protein domains induced by surface recognition. *Biochemistry.* 28:8214–8221.

Brillinger, D. R., K. H. Downing, and R. M. Gleaser. 1990. Some statistical aspects of low-dose electron imaging of crystals. *J. Statist. Planning Inference.* 25:235–259.

Brink, J., and W. Chiu. 1991. Contrast analysis of cryo-images of n-paraffin recorded at 400 kV out to 2.1 Å resolution. *J. Microsc.* 161: 279–295.

Brink, J., and W. Chiu. 1994. Applications of a slow-scan CCD camera in protein electron crystallography. *J. Struct. Biol.* 113:23–34.

Brink, J., M. Sherman, J. Berriman, and W. Chiu. 1994. Charging phenomena observed on biological specimens in a 400 kV electron cryomicroscope. *In* Proceedings of the 52nd Annual Meeting of the Microscopy Society of America, New Orleans. San Francisco Press. 118–119.

Brown, L., and I. F. Trotter. 1956. X-ray studies of poly-L-alanine. *Trans. Faraday Soc.* 52:537–548.

Brünger, A. T. 1992a. X-PLOR. Version. 3.1f. Yale University.

Brünger, A. T. 1992b. Free R value: a novel statistical quantity for assessing the accuracy of crystal structures. *Nature.* 355:472–475.

Bullough, P. A., and R. Henderson. 1990. Phase accuracy in high-resolution electron microscopy of trigonal and orthorhombic purple membrane. *Biophys. J.* 58:705–711.

Cantor, C. R., and P. R. Schimmel. 1980. Biophysical Chemistry. Volume II. Techniques for the Study of Biological Structure and Function. W. H. Freeman and Company, San Francisco. 754 pp.

Chiu, W., and M. F. Schmid. 1993. Electron crystallography of macromolecules. *Curr. Opin. Biotechnol.* 4:397–402.

Darst, S. A., M. Ahlers, P. H. Meller, E. W. Kubalek, R. Blankenburg, H. O. Ribi, H. Ringsdorf, and R. D. Kornberg. 1991. Two-dimensional crystals of streptavidin on biotinylated lipid layers and their interactions with biotinylated macromolecules. *Biophys. J.* 59:387–396.

DeTitta, G. T., J. W. Edmonds, W. Stallings, and J. Donohue. 1976. Molecular structure of biotin. Results of two independent crystal structure investigations. *J. Am. Chem. Soc.* 98:1920–1926.

Fromherz, P. 1971. Electron microscopic studies of lipid protein films. *Nature.* 231:267–268.

Fukami, A., and K. Adachi. 1965. A new method of preparation of a self-perforated micro plastic grid and its application (I). *J. Electron Microsc. (Tokyo).* 14:112–118.

Furano, T., and H. Sasabe. 1993. Two-dimensional crystallization of streptavidin by nonspecific binding to a surface film: study with a scanning electron microscope. *Biophys. J.* 65:1714–1717.

Garlick, R. K., and R. W. Giese. 1988. Avidin binding of radiolabeled biotin derivatives. *J. Biol. Chem.* 263:210–215.

Green, N. M. 1975. Avidin. *Adv. Protein Chem.* 29:85–143.

Haas, H., G. Brezesinski, and H. Möhwald. 1995. X-ray diffraction of a protein crystal anchored at the air/water interface. *Biophys. J.* 68: 312–314.

Hayward, S. B., and R. M. Stroud. 1981. Projected structure of purple membrane determined to 3.7 Å resolution by low temperature electron microscopy. *J. Mol. Biol.* 151:491–517.

Helm, C. A., W. Knoll, and J. N. Israelachvili. 1991. Measurement of ligand-receptor interactions. *Proc. Natl. Acad. Sci. USA.* 88:8169–8173.

Hemming, S. A., A. Bochkarev, S. A. Darst, R. D. Kornberg, P. Ala, D. S. C. Yang, and A. M. Edwards. 1995. The mechanism of protein crystal growth from lipid layers. *J. Mol. Biol.* 246:308–316.

Henderson, R. 1992a. Image contrast in high-resolution electron microscopy of biological macromolecules: TMV in ice. *Ultramicroscopy.* 46:1–18.

Henderson, R. 1992b. AVRGAMPHS. Version 1.3. MRC, Cambridge.

Henderson, R., J. M. Baldwin, K. H. Downing, J. Lepault, and F. Zemlin. 1986. Structure of purple membrane from *Halobacterium halobium*: recording, measurement and evaluation of electron micrographs at 3.5 Å resolution. *Ultramicroscopy.* 19:147–178.

Hendrickson, W. A., A. Pähler, J. L. Smith, Y. Satow, E. A. Merritt, and R. P. Phizackerley. 1989. Crystal structure of core streptavidin determined from multiwavelength anomalous diffraction of synchrotron radiation. *Proc. Natl. Acad. Sci. USA.* 86:2190–2194.

Herron, J. N., W. Müller, M. Paudler, H. Riegler, H. Ringsdorf, and P. A. Suci. 1992. Specific recognition-induced self-assembly of a biotin lipid/streptavidin/Fab fragment triple layer at the air/water interface: ellipsometric and fluorescence microscopy investigations. *Langmuir.* 8:1413–1416.

Hiroshi, E., J. N. Herron, W. Müller, Y. Okahata, H. Ringsdorf, and P. Suci. 1992. Docking of a second functional protein layer to a streptavidin matrix on a solid support: studies with a quartz crystal microbalance. *Angew. Chem. Int. Ed. Engl.* 31:1087–1090.

Holser, W. T. 1958. Point groups and plane groups in a two-sided plane and their subgroups. *Z. Kristallogr.* 110:266–281.

Ibers, J. A., and W. C. Hamilton, editors. 1974a. International Tables for x-ray Crystallography, Vol. I, Symmetry Groups. The Kynoch Press, Birmingham, England. 64.

Ibers, J. A. and W. C. Hamilton, editors. 1974b. International Tables for x-ray Crystallography, Vol. IV, Revised and Supplemental Tables. The Kynoch Press, Birmingham, England. 152–175.

Jap, B. K., M. Sulauf, T. Scheybani, A. Hefti, W. Baumeister, U. Aebi, and A. Engel. 1992. 2D crystallization: from art to science. *Ultramicroscopy.* 46:45–84.

Jeng, T. W., and W. Chiu. 1983. Low dose electron microscopy of the crotoxin complex thin crystal. *J. Mol. Biol.* 164:329–346.

Kornberg, R. D., and S. A. Darst. 1991. Two dimensional crystals of proteins on lipid layers. *Curr. Opin. Struct. Biol.* 1:642–646.

Krivanek, O. L., and P. E. Mooney. 1993. Applications of slow-scan CCD cameras in transmission electron microscopy. *Ultramicroscopy.* 49: 95–108.

Kubalek, E. W., R. D. Kornberg, and S. A. Darst. 1991. Improved transfer of two-dimensional crystals from the air/water interface to specimen support grids for high-resolution analysis by electron microscopy. *Ultramicroscopy.* 35:295–304.

Mooney, P. E., G. Y. Fan, K. V. Truong, D. B. Bui, and O. L. Krivanek. 1990. Slow-scan CCD camera for transmission electron microscopy. *In* Proceedings of the XIIth International Congress of Electron Microscopy, Seattle, WA, Vol. 1. L. D. Peachey and D. B. Williams, editors. San Francisco Press. 164–165.

Morgan, H., and D. M. Taylor. 1992. A surface plasmon resonance immunosensor based on the streptavidin-biotin complex. *Biosensors Bioelectronics.* 7:405–410.

Müller, W., H. Ringsdorf, E. Rump, G. Wildburg, X. Zhang, L. Angermaier, W. Knoll, M. Liley, and J. Spinke. 1993. Attempts to mimic docking processes of the immune system: recognition-induced formation of protein multilayers. *Science.* 262:1706–1708.

Sack, J. 1991. CHAIN: Crystallographic Modeling Program. Version 4.5. Baylor College of Medicine.

Schmid, M. F., R. Dargahi, and M. W. Tam. 1993. SPECTRA: a system for processing electron images of crystals. *Ultramicroscopy.* 48:251–264.

Thon, F. 1971. Phase contrast electron microscopy. *In* Electron Microscopy in Material Science. U. Valdre, editor. Academic Press, New York. 571–590.

Unger, V. M., and G. F. X. Schertler. 1995. Low-resolution structure of bovine rhodopsin determined by electron cryo-microscopy. *Biophys. J.* 68:1776–1786

Uzgiris, E. E., and R. D. Kornberg. 1983. Two-dimensional crystallization technique for imaging macromolecules, with an application to antigen-antibody-complement complexes. *Nature.* 301:125–129.

Weber, P. C., D. H. Ohlendorf, J. J. Wendoloski, and F. R. Salemme. 1989. Structural origins of high-affinity biotin binding to streptavidin. *Science.* 243:85–88.

Weisenhorn, A. L., F.-J. Schmitt, W. Knoll, and P. K. Hansma. 1992. Streptavidin binding observed with an atomic force microscope. *Ultramicroscopy.* 42–44:1125–1132.

Zhou, Z. H., S. Hardt, B. Wang, M. B. Sherman, J. Jakana, and W. Chiu. 1995. CTF determination of images of ice-embedded single particles using a graphics interface. *J. Struct. Biol.* In press.